J O U R N A L O F
Ceramic
Processing Research

A dual-functional gadolinium-conjugated hydroxyapatite nanoparticle-containing curcumin as a potential nanoplatform for bioapplications

Jéssica Pauline Nunes Marinho[a], Marcelo Fernandes Cipreste[b], Alisson Krohling[a] and Edésia Martins Barros Sousa[a],*

[a]*Centro de Desenvolvimento da Tecnologia Nuclear – CDTN – Avenida Presidente Antônio Carlos, 6.627 - Campus UFMG, CEP 31270-901, Belo Horizonte, Minas Gerais Belo Horizonte, Brazil*
[b]*JHS Biomateriais. Rua Ouro Branco, 345 – Sabará, Minas Gerais, Brazil*

Nanomaterials such as hydroxyapatite have been extensively researched, thanks to their unsal properties, which are similar in chemical composition to bone tissue. In addition, hydroxyapatite nanoparticles offer a wide range of possibilities for functionalization which make it an interesting material for target drug delivery applications, showing strong potential for coupling natural substances such as curcumin to improve the antitumor effect of this substance in the fight against cancer. Curcumin has been researched over the years, thanks to its anticancer properties. Hydroxyapatite also allows the incorporation of paramagnetic elements into their structure, such as gadolinium (Gd), allowing the production of a probe for diagnostic imaging using nuclear magnetic resonance imaging systems. In this work, hydroxyapatite nanorods (HA) doped with Gd were synthesized to produce folic acid (FA) functionalized nanostructures for targeted delivery of curcumin (CM). The samples were characterized using various techniques, including Fourier transform infrared spectroscopy (FTIR), UV-visible spectroscopy (UV-Vis), X-ray diffraction (XRD), thermogravimetric analysis (TGA), zeta potential analysis (ζ), transmission electron microscopy (TEM), and vibrating samples magnetometry (VSM). The results indicated a successful obtaining of paramagnetic HA-Gd nanostructures functionalized with FA and CM, exhibiting characteristics that credit this system for future biological assays in order to evaluate their efficiency in the treatment and diagnosis of osteosarcoma.

Keywords: Hydroxyapatite nanorods, Folate functionalization, Theranostics, Magnetic properties, Curcumin.

Introduction

Hydroxyapatite (HA) is one of the most used bioceramics in the repair of damaged regions of the skeletal muscle system [1]. Its similarity with the inorganic phase of tissues such as bones and teeth give it biocompatibility, low toxicity, and osteoconductive properties, which allow its use in different biological applications [2-6]. From the chemical composition point of view, the biological hydroxyapatite differs from the synthetic one for being carbonated and presenting a non-stoichiometric composition, with the presence of different ions in its structure [2]. Special properties such as the high stability and flexibility of this material are responsible of possible cationic and anionic substitutions [7, 8]. Moreover, the possibility of obtaining nanoscale particles with different morphologies allows the multifunctional use of this bioceramic as a drug carrier and contrast agent in diagnostic imaging [9].

Recently, the synthesis of rare earth doped nanoparticles has attracted considerable attention due to their promising multifunctional applications in biomedical imaging [8]. Gadolinium (Gd) based contrast media have been used in clinical practice for nuclear magnetic resonance imaging (NMRI) [11]. Gadolinium is one of the paramagnetic rare earth elements of the lanthanide series. This element can enhance NMRI images mainly by reducing the T1 relaxation time in the tissues in which it is located [12]. According to Bartolini et al. [12], an interesting feature is that Gd can be activated in a nuclear reactor to generate the radioisotope [159]Gd, a beta and gamma radiation emitter, which allows diagnosis by magnetic resonance imaging and by single photon emission computed tomography (SPECT).

The compounds approved as NMRI contrast agents for human use are in the form of non-toxic gadolinium metalorganic complexes such as gadobutrol, gadodiamide, and gadoterate meglumine. However, Gd^{3+} ions can detach from the chelates and when free in the bloodstream is highly toxic and can disperse into bone tissue and the liver causing liver necrosis [13]. Patients with renal dysfunction can induce nephrogenic systemic fibrosis (NSF) [14, 15]. Recent studies show that in the long term, individuals with normal renal function exposed to gadolinium-based contrast agents exhibit Gd^{3+} accumulation in bone tissues and organs such as the kidney, brain, skin, bone, and liver, associated

*Corresponding author:
 Tel : +55 (31) 3469-9523
 Fax: +55 (31) 3469-9344
 E-mail: sousaem@cdtn.br

with repeated exposure to contrast agents that at high levels contribute to the emergence of encephalopathies [13, 16, 17].

In this sense, the production of hydroxyapatite nanoparticles doped with Gd may be an alternative to the toxicity problems. In vitro tests have evaluated the effects of HA particles doped with gadolinium on the viability of bone marrow stem cells. The results showed high protein adsorption capacity and high cell viability demonstrating its potential for applications in biomedical fields [18]. Considering gadolinium-conjugated hydroxyapatite nanoparticle and its applications, Cipreste et al. [19] demonstrated that functionalization of Gd substituted HA with folic acid creates a well-organized active targeting for osteosarcomas, which overcomes concerns associated with current approaches to bone tumor treatment and diagnosis. Folic acid, a water-soluble vitamin, stands out as an essential substance in cell division and nucleotide synthesis. Furthermore, folate receptors are present in almost all tissues, but they are overexpressed in several types of cancer, while their expression is limited in healthy tissues and organs [20]. Folic acid and folate conjugates bind to FR-α and FR-β receptors with high affinity and enter RF-expressing cells by receptor-mediated endocytosis. A cellular uptake and cytotoxicity study performed on human cervical cancer cell lines (Hela) and human lung cancer cell lines (A-549) showed facilitated uptake of nanoparticles by folate receptors [21]. Thus, folic acid is a promising selective driver of drug nanocarriers to tumor regions [20].

Gd-substituted HA has also shown potential for applications in cancer therapy as a drug carrier. In one study, gadolinium-doped and polyethyleneimine-modified hydroxyapatite nanorods showed high loading capacity for doxorubicin and a pH-responsive drug release capacity, and excellent T1-weighted NMRI properties [14]. To confer therapeutic properties, in addition to chemotherapeutics, various natural products have been used to treat diseases or develop new drugs. Recent works has demonstrated that thanks to advances in nanotechnology, improved nanostructures offer the unique possibility of transport, protection, and delivery of potential therapeutic molecules to specific targets [22]. Curcumin, the main bioactive component of Curcuma Longa L, also known as turmeric, has been used to treat diseases in traditional Chinese medicine and Ayurveda for over 2,000 years [23]. Curcumin has the potential to prevent and/or control various diseases, such as cardiovascular, neurological, autoimmune, hepatic, and gastrointestinal diseases, including cancer [24, 25]. Victorelli et al. [26] developed a liquid crystalline system as a medium for the formulation and administration of curcumin for the treatment of cervical cancer. Results demonstrated biocompatibility for L929 cells and toxicity for Hela cells. In addition, they also evaluated vascular changes in response to treatment and observed

that the caliber and number of vessels decreased after the application of curcumin-loaded formulations. In another study, both curcumin and nanocurcumin were shown to reduce the viability of HepG2 and Huh-7 cancer cells. Furthermore, in the mouse test, curcumin and nanocurcumin were able to reduce the systemic release of liver enzymes and reverse acrylamide-induced oxidative stress [27].

Thus, the present work aims at the synthesis and characterization of a multifunctional nanosystem synthesized from gadolinium-doped hydroxyapatite nanoparticles functionalized with folic acid for targeted delivery of curcumin as a potential anticancer agent. In addition, it is well established that curcumin strongly chelates several metal ions, so its use in conjunction with gadolinium-doped hydroxyapatite may represent an added safety in the use of these particles as contrast agents. This initial study contributes to the search for developing safer and more efficient nanostructures, capable of acting as contrast agents in the acquisition of images for cancer diagnosis and therapy.

Materials and Methods

Materials

Hexadecyltrimethylammonium bromide (CTAB - $C_{14}H_{42}N.Br$) (Sigma-Aldrich), calcium nitrate tetrahydrate, $Ca(NO_3)_2.4H_2O$, (Sigma-Aldrich), potassium phosphate dibasic trihydrate, $K_2HPO_4.3H_2O$, (Sigma-Aldrich), ammonium hydroxide (NH_4OH), curcumin - CM (Sigma-Aldrich), 3-amino-propyltriethoxysilane - APTES (Sigma-Aldrich), folic acid (Sigma-Aldrich), gadolinium nitrate (Sigma-Aldrich), acetic acid P.A. (Neon).

Synthesis of hydroxyapatite nanorods

Hydroxyapatite nanorods were prepared according to previously published work [19, 28]. The synthesis used is based on the surfactant-assisted hydrothermal method, which consists of the preparation of two solutions, one containing calcium nitrate and CTAB and the other containing dibasic potassium phosphate trihydrate. The pH of both solutions was corrected to 11 with the addition of ammonium hydroxide and the solution containing the phosphate ions was added dropwise to the calcium precursor solution. At the end of dripping, the resulting suspension was kept stirring for 14 hours at room temperature. The obtained suspension was then transferred to the reactor and subjected to hydrothermal treatment at 100 °C for 10 hours. After hydrothermal treatment, the material was centrifuged, filtered, and washed with deionized water and ethanol and subsequently dried in an oven at 60 °C for 24 hours. Finally, the material was calcined for 6 hours at 600 °C and identified as HA.

Synthesis of gadolinium-doped hydroxyapatite

For the synthesis of hydroxyapatite (HA) doped with

gadolinium ions, identified as HAGd, 7.5% of the molar amount of Ca^{2+} ions were replaced by Gd^{3+} ions by adding gadolinium nitrate in the synthesis but maintaining the calcium + gadolinium molar concentration in 0.167 $mol.L^{-1}$. Solution (I) was obtained from the dissolution of calcium nitrate and gadolinium nitrate. Solution (II) was prepared by completely dissolving CTAB in deionized water, followed by the addition of dibasic potassium phosphate trihydrate (0.1 $mol.L^{-1}$). The pH of the solution was adjusted to 11 with the addition of ammonium hydroxide. Solution (I) was added dropwise to the solution (II) and stirred for 14 h. The hydrothermal treatment was carried out using the same methodology used in the preparation of HA, as well as the filtering and drying process.

Synthesis of HAGd-CMAP nanostructures

To incorporate CM into HAGd nanoparticles, the modified CM called CMAP was first obtained. The modification was carried out through the reaction of 1 mmol of CM and 4 mmol of APTES in an acidic medium at 75 ºC for 24 h, under constant stirring, in a reflux system with an inert atmosphere [28]. The resulting solution was lyophilized to obtain the powdered material. To incorporate CMAP into HAGd, both components were added in a mass ratio of 1:1 in 50 ml of deionized water and kept under stirring for 24 h at 50 ºC. The resulting material was filtered and washed with deionized water and excess ethanol and then dried in an oven at 60 °C for 24 hours. The nanostructure obtained was identified as HAGd-CMAP.

Functionalization process of HAGd-CMAP nanostructures with folic acid

As in the previous process, for the incorporation of folic acid (FA), a mixture of HAGd-CMAP and FA was made in a 1:1 mass ratio in 50 ml of deionized water. The mixture was kept under vigorous stirring for 24 hours at 50 °C. The resulting powder was collected under vacuum filtration and washed with deionized water and excess ethanol. Subsequently, the material was dried in an oven at 60 °C for 24 hours. The nanostructure obtained was identified as HAGd-CMAP-F.

Characterizations

The synthesized samples were characterized by X-ray diffraction, using the powder method, with copper Kα radiation, and a wavelength (λ) equal to 1.54178 Å. The diffractograms were obtained using Rigaku equipment, Japan, and measurements were made using a goniometer speed of 0.4º/min. The ICSD 16742 Database was used to identify the HA phase. Transmission electron microscopy (TEM) was used to evaluate the morphological characteristics of the systems (Tecnai G2-12 – Spirit Biotwin FEI – 120 kV from the Microscopy Center of the Federal University of Minas Gerais - UFMG). The presence of functional groups, as well as the chemical composition of the samples, was verified using Fourrier Transform Infrared Spectrophotometry (FTIR). Infrared spectra covering the region of 4000-400 cm^{-1} were obtained by the Nicolet 6700 spectrophotometer (Thermo Scientific, USA), with a resolution of 4 cm^{-1} to 64 $scans.min^{-1}$. Thermogravimetric analysis (TGA) was performed on a DTG-60H analyzer (Shimadzu, Japan) at 25 to 800 °C with a heating rate of 10 °C min^{-1}. The UV-Visible Spectroscopy (UV-VIS) technique was used to identify curcumin in the HAGd-CMAP and HAGd CMAPF samples. For the test, the samples were dispersed in dimethyl sulfoxide with the aid of an ultrasound bath for 10 minutes. The assay was performed on the UV-2550 spectrophotometer (Shimadzu, Japan). Zeta potential from Malvern Instruments analysis was used to evaluate the stability of nanomaterials when dispersed in a liquid medium. Samples were prepared with concentrations of 0.05 mg/mL in Milli-Q® water. To promote the dispersion of particles in the water, the samples were ultrasonified in a tip ultrasound with an energy of 10 kJ, for approximately 30 minutes. Magnetic characteristics of the samples were performed by vibrating sample magnetometry (VSM, 7400 series, LakeShore Cryotronics, USA).

Results and Discussions

X-ray Diffraction (XRD)

The XRD technique was conducted to characterize the crystallographic phases that compose the synthesized samples. The diffractograms are shown in Fig. 1 and exhibit only crystallographic phases that are characteristic of the hydroxyapatite hexagonal structure with space group p_{63}/m, according to the Powder Diffraction File 16742 from ICSD database, evidencing the planes (0 0 2), (2 1 1), (3 0 0) and (2 0 2) through peaks at approximately 25,8; 31,7; 32,2 and 32,9 2θ angles showing typical crystallinity degree of hydroxyapatite nanoparticles. These findings indicate that, within the limit of detection of the technique, the amount of gadolinium ions introduced during the HAGd synthesis does not prevent the hydroxyapatite formation and the synthesis conditions do not favor the precipitation of any gadolinium crystallographic phase, in agreement with the literature [16, 26]. The incorporation of Gd in the HAGd sample was evidenced by other techniques such as XPS and VSM whose results are shown in the following topics. Furthermore, Gd ions caused shrinkage of nanocrystallite (21,1 ± 5 nm and 15,3 ± 5 nm for HA and HAGd75, respectively) as evidenced by calculations applying the Scherrer equation:

$$\beta_s(2\theta)_{hkl} = \frac{k\lambda}{T cos\theta_{hkl}},$$

where β_s is the HWHM in radians (6.83×10^{-3} and
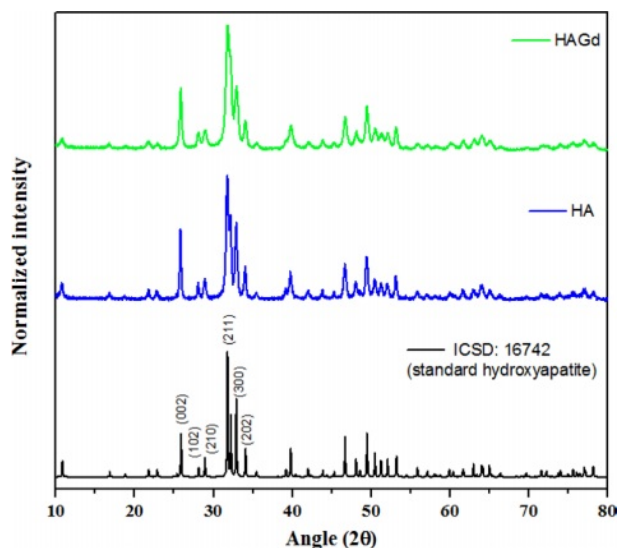
Fig. 1. X-ray diffractograms for ICSD samples: 16742 (standard hydroxyapatite) and HA and HAGd.

9.44×10^{-3} for HA and HAGd, respectively), λ is the X rays wavelength (0.154 nm), K is a constant near unity (0.9) and T is the average thickness of the crystal (in nm) in a direction normal to the mean diffracting plane (2 1 1) (2θ = 31,75 and 31,81 for HA and HAGd, respectively). The shrinkage of the nanocrystallite in the Gd-doped sample is possibly associated with the reduction in the sizes of the nanoparticles as evidenced by the particle sizes distribution measured through TEM images (shown in the next topic) and was probably caused by a disturbing or alterations in the mechanism of nucleation and growth of the crystals.

Transmission electron microscopy – TEM
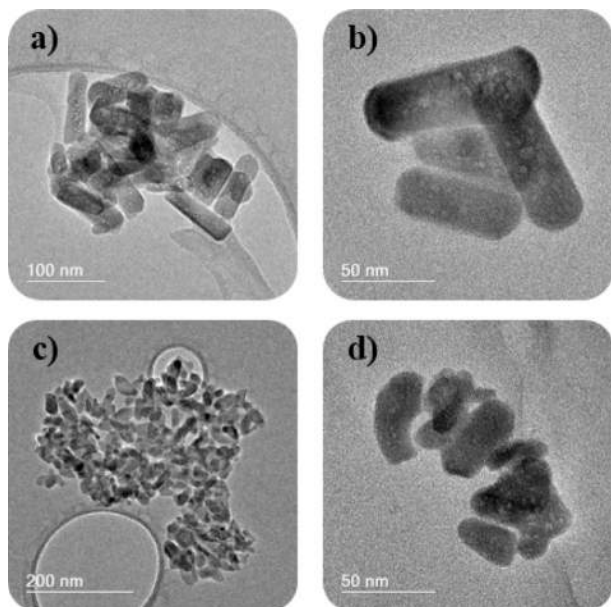
Fig. 2. TEM images of (a,b) HA and (c,d) HAGd.

The morphology and size of the particles were investigated by TEM and are presented in Fig. 2. The presence of pores along the structure was observed in both samples. The HA sample (Fig. 2a and 2b) showed the morphology of nanorods with an average size of 108±29 nm in length and 28±6 nm in width. On the other hand, the gadolinium-doped sample (Fig. 2c and 2d) showed a more rounded morphology and smaller dimensions, in agreement with the data obtained by XRD. The average particle size was 39±6 nm in length and 16±1 nm. Similar results were obtained by Mondal and colleagues [8] in a study on the doping of hydroxyapatite with rare earth elements. The authors observed a smaller particle size distribution in the Gd-doped sample compared to pure hydroxyapatite and in the europium-doped sample.

Zeta Potential – ζ

The surface chemical properties of the nanoparticles were characterized by measuring the ζ potential in MilliQ water with pH 6.0. HA and HAGd samples showed negative ζ potential (Table 1), with no significant difference. Close values were already expected since, in the doping process, there is a charge compensation so it is possible to replace Ca^{2+} ions with Gd^{3+} dopant ions. This compensation occurs by the generation of vacant cationic sites or by the loss of a proton from OH^- to provide an O^{2-} ion [9, 30]. With the addition of curcumin in the HAGd samples, there was an increase in the ζ potential (-6.5±0.2 mV) due to the protonation of the amine groups of APTES that acts as a coupling agent for inserting this moiety in the CM structure so that it could interact with HA. After functionalization with FA, the ζ potential showed a reduction and reached the lowest negative value (-15.5±0.7 mV). This change can be attributed to the presence of existing acid groups in its chemical structure since OH^- groups ionize in O^{-2} and H^+ in aqueous dispersion at neutral pH.

The changes in the values of the zeta potentials of the samples are a strong indication of an effective surface modification, indicating that the final HAGd-CMAP-F was successfully functionalized.

Fourier transform infrared spectroscopy – FTIR

The FTIR spectra of the synthesized samples are shown in Fig. 3. In the HA and HAGd spectra,

Table 1. Zeta potential measurements of HA, HAGd, HAGd-CMAP, and HAGd-CMAP-F samples.

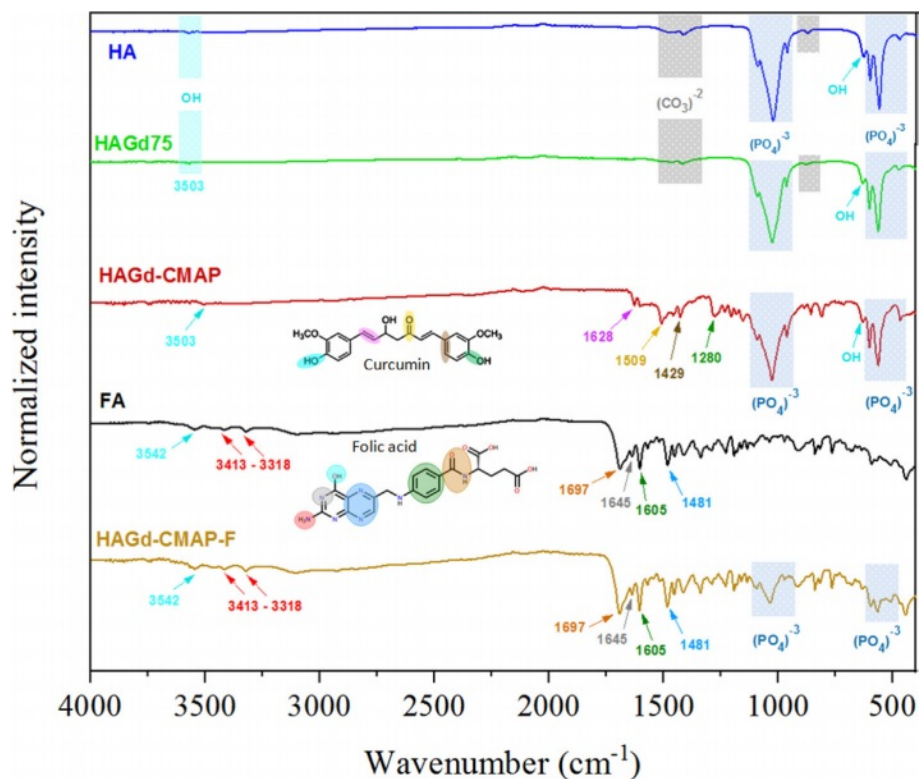| Sample	Zeta Potential (mV)±SD
HA	-10.9±0.2
HAGd	-12.0±0.7
HAGd-CMAP	-6.5±0.2
HAGd-CMAP-F	-15.5±0.7

Fig. 3. FTIR spectra of HA, HAGd, HAGd-CMAP, and HAGd-CMAP-F.

the presence of the main characteristic bands of hydroxyapatite [4-6, 19, 31, 32] can be noted. The main signal of the phosphate group appears at 1091 cm^{-1} and 1031 cm^{-1}, which represents the vibration of the asymmetric axial deformation of the P-O bond. Bands at 962, 601, 565, and 474 cm^{-1} are attributed, respectively, to the symmetric axial deformation of the P-O bond of the phosphate groups, to the symmetric angular deformation of the P-O-P bond and to the asymmetric angular deformation of the P-O-P bond. Symmetric axial and angular strain vibrations of hydroxyl groups appear at 3572 cm^{-1} and 632 cm^{-1} [33-35]. Vibrational modes related to the presence of carbonate are also observed. The bands at 1448 and 1415 cm^{-1} are related to the symmetrical axial strain of the $(CO_3)^{-2}$ group and the band at 877 cm^{-1} to out-of-plane angular strain [36, 37]. The presence of these bands characterizes the obtainment of carbonated hydroxyapatite with partial replacement of the phosphate groups by carbonate, which can be classified as type B substitution. This type of substitution is associated with the synthesis of hydroxyapatite by wet methods at low temperatures, which justifies such a finding [31, 38-40]. In general, from the spectra, it was not possible to observe a significant change after doping with gadolinium. There was also no evidence of the formation of new calcium phosphate phases.

The main difference in the spectrum of the HAGd-CMAP sample is the presence of bands from curcumin, thus indicating its presence in the nanostructure. The band at 3503 cm^{-1} is attributed to the axial deformation of the phenolic hydroxyl. At 1628 cm^{-1}, the axial strain bands of the carbonyl C=O bond and the aromatic ring C=C bonds overlap [41, 42]. Carbonyl-only axial deformation was assigned to the band at 1508 cm^{-1} [43]. The in-plane angular strain vibration of the C-C-C, C-C-H, and C-O-H bonds of the aromatic ring was attributed to the band at 1429 cm^{-1}. At 1280 cm^{-1} the band is located due to the vibration of the C-O bond of the enol group [44].

The HAGd-CMAP-F nanostructure spectrum showed the main AF characteristic bands at 1697, 1645, 1605, and 1481 cm^{-1}. These bands correspond respectively to the amide group, axial deformation of the benzene ring, angular deformation of the N-H bond, and axial deformation of the hetero ring [19, 45]. It was not possible to observe the bands previously attributed to curcumin, possibly due to an overlapping of the folic acid bands. In addition, there is a reduction in the intensity of the bands related to the hydroxyapatite phosphate group. This result indicates that possibly a large amount of FA was incorporated into the sample.

Thermogravimetric Analysis (TG)

Thermogravimetric analysis was carried out to evaluate the thermal stability of the samples and to investigate the effectiveness of the process of curcumin incorporation and functionalization with folic acid. The results are shown in Fig. 4 and Table 2. Within the

Table 2. Weight loss percentages obtained through thermogravimetry analysis of different samples.

| Temperature range (°C)	Weight loss (%)			
	HA	HAGd	HAGd-CMAP	HAGd-CMAP-F
25-150	0.8	1.4	1.0	7.0
150-400	2.5	2.8	17.1	27.6
400-700	1.2	1.4	17.2	45.7
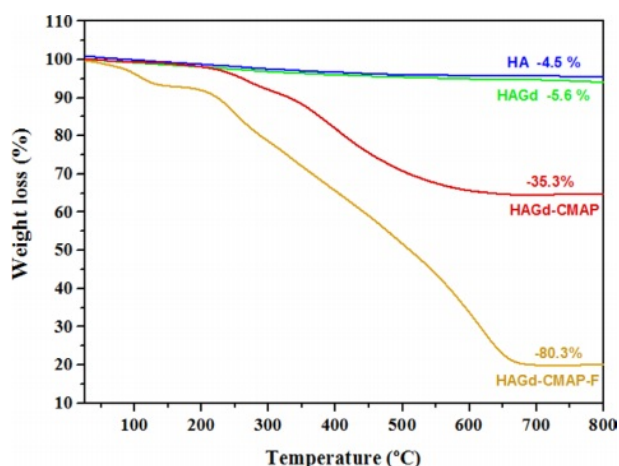
Fig. 4. Thermogravimetric curve of the HA, HAGd, HAGd-CMAP, and HAGd-CMAP-F samples.

temperature range studied, the HA and HAGd samples showed high thermal stability with mass losses of 4.5%

and 5.6% respectively. These small mass losses can be attributed to the evaporation of adsorbed water and residual molecules from the synthesis process. The HAGd-CMAP sample exhibited a similar mass loss profile over the temperature range from 25 to 150 °C. However, a significant increase in mass loss is observed from 215 °C to approximately 700 °C, resulting in a total mass loss of 35.3% that can be associated with curcumin degradation. The thermogravimetric curve of the HAGD-CMAP-F sample shows a mass loss of 80.3%. This increase in mass loss evidences the functionalization of nanoparticles with a large amount of folic acid, corroborating the results obtained in FTIR.

UV-Vis Spectroscopy

The pharmacological and biological properties attributed to curcumin are closely related to its chemical structure, which is presented in the form of diketone and keto-enol (Fig. 5a). Its structure has three "acid" protons, two phenolic and one enolic proton. Its low
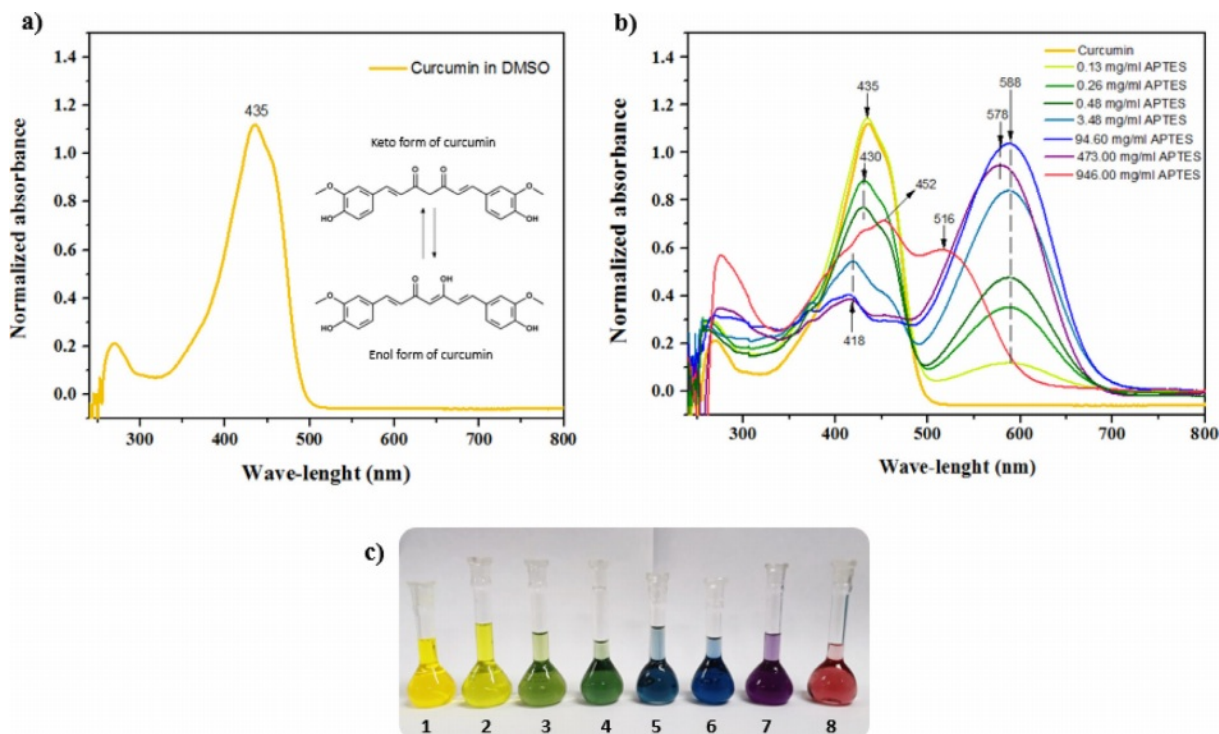
Fig. 5. a) Absorption spectra of curcumin (0.008 mg/ml) in DMSO; b) Absorption spectra of curcumin in DMSO with APTES concentrations of 0, 0.13, 0.26, 0.48, 3.48, 94.60, 473.0 and 946.0 mg/ml, respectively; c) Photograph of the curcumin solutions in DMSO with different concentrations of APTES, used to obtain the absorption spectra.

aqueous solubility is the main obstacle to its use for the treatment of diseases. Several studies aimed at increasing the solubility and bioavailability of curcumin. The modification of the CM with APTES had the main objective to allow its anchorage in the HAGd nanoparticles. However, it is known that in an alkaline environment, curcumin undergoes deprotonation and rapidly degrades [23, 46, 47]. Knowing the basic character of APTES, a study of the behavior of CM in dimethylsulfoxide (DMSO) at different concentrations of APTES was carried out to evaluate the characteristics of the material obtained after the reaction.

Figs. 5b and 5c show the absorption spectra of CM in DMSO with different concentrations of APTES and the photograph of the solutions with different colors. In the spectrum, the maximum absorption at 435 nm is associated with the CM in its neutral phase and corresponds to Solution 1. With the sequential increase of the APTES concentration, it is possible to observe the appearance of an isobastic point at 498 nm and a new absorption band at 588 nm (Fig. 5b and 5c - Solutions 2-7). This absorption is related to the deprotonated form of CM. As the APTES concentration increases further, a hypsochromic shift of the isobastic point (488 nm) and maximum absorption (578 nm) occurs, which can be associated with doubly deprotonated CM and the curve represented in red (Fig. 5b) can be associated with triply deprotonated CM (Fig. 5b and 5c - solution 8) [48]. The different stains obtained due to the different concentrations of APTES may be associated with the redistribution of the negative charge on the CM molecule, which may lead to the formation of quinoid structures in the phenolic fragments of the intermediate deprotonated forms [48]. Comparing these results with the spectrum of the HAGd-CMAP sample (Fig. 6), it was possible to observe that its absorption spectrum is similar to that of CM in its neutral form. This is an indication that the modification process with APTES was efficient to anchor the CM in the nanostructures
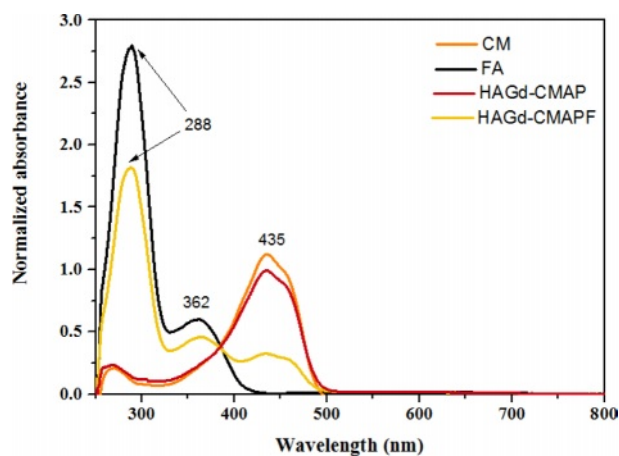

Fig. 6. Absorption spectra of samples of curcumin (CM), folic acid (FA), HAGd-CMAP, and HAGd-CMAP-F in DMSO.
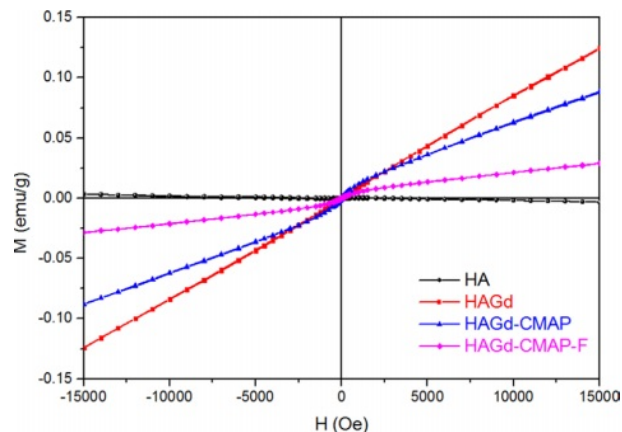

Fig. 7. Magnetic properties obtained by magnetometry of vibrating sample, of undoped and Gd-doped HA samples, with curcumin and folic acid.

without causing alteration in its structure that would lead to its degradation. In the HAGd-CMAP-F spectrum (Fig. 6), in addition to the absorption band at 435nm, it is possible to observe the presence of absorption bands at 288 nm and 362 nm associated with the presence of folic acid, indicating the effectiveness of the functionalization [49].

Vibrating Sample Magnetometry – VSM

Vibrating samples magnetometry (VSM) measurements were carried out at room temperature to study the magnetic properties of hydroxyapatite (HA) samples, doped with Gd, curcumin (CMAP), and folic acid (FA). The results in Fig. 7 showed the diamagnetic signal of the pure HA sample ($\chi < 0$), while the samples with the incorporation of Gd in the matrix showed a paramagnetic signal (PM) ($\chi > 0$) [19]. Although attenuated by the dilution of the Gd mass after the incorporation and functionalization step, as expected, the paramagnetic behavior of the developed nanoplatform (sample HAGd-CMAP-F) should allow for the use as an MR contrast agent [48], while contributing to better biocompatibility [50].

One of the main uses of HA doped with the paramagnetic ion of Gd^{3+} is its simultaneous application in magnetic resonance imaging (MRI) and computed X-ray tomography (CT) [29, 51, 52]. The MRI technique is widely used for non-ionizing imaging that offers high contrast and spatial resolution of soft tissues and interfaces such as bone tissue. It is useful for diagnosing soft tissue injuries such as herniated discs and sports injuries, and it is also good for identifying tumors. It is also known that replacing small amounts of Ca^{2+} ions from the HA structure can contribute to lattice disorder, reduce particle size and decrease crystallinity by affecting the luminescent properties of HA, which can be adjusted by replacing these Ca^{2+} ions divalent by different rare earth luminescent elements such as Gd, Dy, Eu, etc. [51].

Conclusion

In this work, the surface functionalization with folic acid of hydroxyapatite nanorods (HA) doped with Gd was achieved for the targeted delivery of curcumin. The HAGd-CMAP-F sample showed magnetic properties with the potential for diagnostic application. The method used to modify curcumin allowed its incorporation into HAGd nanoparticles, which can confer a therapeutic action on the nanostructure. In addition, the functionalization of the HAGd nanorods with folic acid can provide active targeting to osteosarcomas, crediting these nanorods for extensive biological assays to study the efficiency of this system to accumulate selectively into the osteosarcoma cells. The developed nanoplatform exhibits promising characteristics that qualify them for future biological tests, to evaluate their biocompatibility and effectiveness for cancer treatment and diagnosis.

Acknowledgments

References

1. K. Kala, M.S. Ganeasan, V. Balasubramani, J. Manovasuki, K. Valivittan, M.R. Kuppusamy, and T.M. Sridhar, J. Ceram. Process. Res. 21[2] (2020) 240-248.
2. C. Tatar, D. Bagci, and O. Kaygili, J. Ceram. Process. Res. 17[5] (2016) 426-429.
3. S. Panda, C.K. Biswas, and S. Paul, Ceram. Int. 47 (2021) 28122-28144.
4. J. Rohana, D. Thenmuhilb, R. Umapriyac, and D. Varatharajan, J. Ceram. Process. Res. 23 (2022) 22-28.
5. D. Leea, D. Kima, B. Kimb, J. Parkc, and J. Leec, J. Ceram. Process. Res. 19 (2018) 15-19.
6. K. Goha, Y. Wonga, R. Singha, H. Chandranc, S. Wongd, and K. Sara Lee, J. Ceram. Process. Res. 23[2] (2022) 158-164.
7. I.R. Gibson, in: M.J.Y. Wagner, William R., Guigen Zhang, Shelly E. Sakiyama-Elbert (Ed.), Biomater. Sci., Fourth Edi, Elsevier, 2020: pp. 307-317.
8. S. Mondal, V.T. Nguyen, S. Park, J. Choi, T.M. Thien Vo, J.H. Shin, Y.H. Kang, and J. Oh, Ceram. Int. 46 (2020) 29249-29260.
9. T. Tite, A.C. Popa, L.M. Balescu, I.M. Bogdan, I. Pasuk, J.M.F. Ferreira, and G.E. Stan, Materials (Basel). 11 (2018) 1-62.
10. H. Li, Y. Zeng, H. Zhang, Z. Gu, Q. Gong, and K. Luo, J. Control. Release. 329 (2021) 482-512.
11. M.E. Bartolini, J. Pekar, D.R. Chettle, F. McNeill, A. Scott, J. Sykes, F.S. Prato, and G.R. Moran, Magn. Reson. Imaging. 21 (2003) 541-544.
12. B. Nasiri-Tabrizi, W.J. Basirun, C.H. Yeong, and W.M. Thein, Ceram. Int. 49 (2023) 7142-7179.
13. E. Akbas, F. Unal, and D. Yuzbasioglu, J. Appl. Toxicol. 43 (2022) 958-972.
14. Y. Liu, Y. Tang, Y. Tian, J. Wu, J. Sun, Z. Teng, S. Wang, and G. Lu, ACS Appl. Nano Mater. 2 (2019) 1194-1201.
15. S. Khairnar, N. More, C. Mounika, and G. Kapusetti, J. Med. Imaging Radiat. Sci. 50 (2019) 575-589.
16. M. Mathur, J.R. Jones, and J.C. Weinreb, Radiographics. 40 (2020) 153-162.
17. A. Al-Muhanna, Saudi J. Med. Med. Sci. 10 (2022) 12.
18. S. jun Yuan, X. yi Qi, H. Zhang, L. Yuan, and J. Huang, Chem. Biol. Interact. 346 (2021).
19. M.F. Cipreste, A.M. Peres, A.A.C. Cotta, F.H. Aragón, A. de M. Antunes, A.S. Leal, W.A.A. Macedo, and E.M.B. de Sousa, Mater. Chem. Phys. 181 (2016) 301-311.
20. N. Ma, M.H. Kwon, S. Palanisamy, Y. Ge, Y. Zhang, F. Kou, L. Dae-Hee, D.J. Lee, I.S. Shin, and S.G. You, Carbohydr. Polym. 304 (2023) 120454.
21. M. Abbasi, M. Sohail, M.U. Minhas, A. Mahmood, S.A. Shah, A. Munir, and M.U.R. Kashif, Int. J. Biol. Macromol. 233 (2023) 123585.
22. J.K. Patra, G. Das, L.F. Fraceto, E.V.R. Campos, M.D.P. Rodriguez-Torres, L.S. Acosta-Torres, L.A. Diaz-Torres, R. Grillo, M.K. Swamy, S. Sharma, S. Habtemariam, and H.S. Shin, J. Nanobiotechnology. 16 (2018) 1-33.
23. L.D. Dias, K.C. Blanco, I.S. Mfouo-Tynga, N.M. Inada, and V.S. Bagnato, J. Photochem. Photobiol. C Photochem. Rev. 45 (2020) 100384.
24. A. Amalraj, A. Pius, S. Gopi, and S. Gopi, J. Tradit. Complement. Med. 7 (2017) 205-233.
25. S. Mukherjee, J.N.E. Baidoo, A. Fried, and P. Banerjee, Biochem. Pharmacol. 176 (2020).
26. F.D. Victorelli, G.M.F. Calixto, K.C. dos Santos, H.H. Buzzá, and M. Chorilli, J. Mol. Liq. 325 (2021).
27. M.M. Atia, H.S. Abdel-Tawab, A.M. Mostafa, and S.A. Mobarak, Sci. Rep. 12 (2022) 1-17.
28. J.P.N. Marinho, N.P. Neme, M.J. de S. Matos, R.J.C. Batista, W.A. de A. Macedo, P.L. Gastelois, D.A. Gomes, M.A. Rodrigues, M.F. Cipreste, and E.M.B. de Sousa, Ceram. Int. 49 (2023) 19932-19949.
29. N.L. Ignjatović, L. Mančić, M. Vuković, Z. Stojanović, M.G. Nikolić, S. Škapin, S. Jovanović, L. Veselinović, V. Uskoković, S. Lazić, S. Marković, M.M. Lazarević, and D.P. Uskoković, Sci. Rep. 9 (2019) 1-15.
30. J.F. Cawthray, A.L. Creagh, C.A. Haynes, and C. Orvig, Inorg. Chem. 54 (2015) 1440-1445.
31. R.C.R. dos Apostolos, M.F. Cipreste, R.G. de Sousa and E.M.B. de Sousa, J. Nanoparticle Res. 22 (2020).
32. L.A.F. Vieira, I.B. da C.J. Meireles, and E.M.B. Sousa, J. Ceram. Process. Res. 23 (2022) 725-736.
33. S. Jose, M. Senthilkumar, K. Elayaraja, M. Haris, A. George, A.D. Raj, S.J. Sundaram, A.K.H. Bashir, M. Maaza, and K. Kaviyarasu, Surfaces and Interfaces. 25 (2021) 101185.
34. V. Prakash, I. Venda, and V. Thamizharasi, Mater. Today Proc. 51 (2022) 1788-1792.
35. X. Song, X. Liu, Y. Ma, Q. Zhu, and M. Bi, Front. Bioeng. Biotechnol. 10 (2022) 1-16.
36. C. Suresh Kumar, K. Dhanaraj, R.M. Vimalathithan, P. Ilaiyaraja, and G. Suresh, J. Asian Ceram. Soc. 8 (2020) 416-429.
37. I.V. Fadeeva, D.V. Deyneko, K. Barbaro, G.A. Davydova, M.A. Sadovnikova, F.F. Murzakhanov, A.S. Fomin, V.G.

Yankova, I.V. Antoniac, S.M. Barinov, B.I. Lazoryak, and J. V. Rau, Nanomaterials. 12 (2022) 852.

38. A. Ressler, A. Žužić, I. Ivanišević, N. Kamboj, and H. Ivanković, Open Ceram. 6 (2021) 100122.
39. R.Z. LeGeros, O.R. Trautz, E. Klein, and J.P. LeGeros, Experientia. 25 (1969) 5-7.
40. F. Yao, J.P. LeGeros, and R.Z. LeGeros, Acta Biomater. 5 (2009) 2169-2177.
41. E.H. Ismail, D.Y. Sabry, H. Mahdy, and M.M.H. Khalil, J. Sci. Res. 6 (2014) 509-519.
42. K.D.C. Perera, G.K. Weragoda, R. Haputhanthri, and S.K. Rodrigo, Vib. Spectrosc. 116 (2021).
43. N.A.N. Hanafy, Int. J. Biol. Macromol. 182 (2021) 1981-1993.
44. G. Verma, A. Gajipara, S.B. Shelar, K.I. Priyadarsini, and P.A. Hassan, J. Drug Deliv. Sci. Technol. 66 (2021) 102769.
45. A.S.Y. Mohammed, A.K.F. Dyab, F. Taha, and A.I.A. Abd El-Mageed, Mater. Sci. Eng. C. 128 (2021).
46. K.I. Priyadarsini, Molecules. 19 (2014) 20091-20112.
47. Z. Moussa, M. Chebl, and D. Patra, J. Photochem. Photobiol. B Biol. 173 (2017) 307-317.
48. Y.B. Tsaplev, V.A. Lapina, and A.V. Trofimov, Dye. Pigment. 177 (2020) 108327.
49. O. Modupe, J.B. Maurras, and L.L. Diosady, J. Agric. Food Res. 2 (2020) 100060.
50. Z. Liu, Q. Wang, S. Yao, L. Yang, S. Yu, X. Feng, and F. Li, Ceram. Int. 40 (2014) 2613-2617.
51. B. Demirel, E. Saban, A. Yaras, and F. Akkurt, J. Asian Ceram. Soc. 9 (2021) 865-873.
52. M. Somoza, R. Rial, Z. Liu, I.F. Llovo, R.L. Reis, J. Mosqueira, and J.M. Ruso, Nanomaterials. 13 (2023) 501.